

# Hybrid diamond quantum sensor with submicrokelvin resolution under ambient conditions

Musang Gong<sup>1,2,†</sup>, Jiahe Xu,<sup>1,2,‡</sup> Min Yu,<sup>1,2,‡</sup> Liyin Zhang,<sup>1,2</sup> Qipeng Li,<sup>1,2</sup> Ning Wang<sup>1,2,\*</sup> and Jianming Cai<sup>1,2,3,†</sup>

<sup>1</sup> School of Physics, Hubei Key Laboratory of Gravitation and Quantum Physics, Institute for Quantum Science and Engineering, Huazhong University of Science and Technology, Wuhan 430074, China

<sup>2</sup> International Joint Laboratory on Quantum Sensing and Quantum Metrology, Huazhong University of Science and Technology, Wuhan 430074, China

<sup>3</sup> Shanghai Key Laboratory of Magnetic Resonance, East China Normal University, Shanghai 200062, China

(Received 10 October 2023; revised 6 February 2024; accepted 7 February 2024; published 27 February 2024)

Nitrogen-vacancy ( $N-V$ ) centers in diamond are promising quantum sensors due to their ultralong coherence time under ambient conditions and multimodal sensing capability.  $N-V$  centers are strongly coupled to magnetic fields, leading to unprecedented sensitivity in magnetic field sensing. However, the coupling strengths between  $N-V$  centers and other crucial parameters, such as temperature and pressure, are not as strong as that of the magnetic field, resulting in a relative low sensitivity. A previous study showed that the temperature sensitivity of a diamond quantum sensor could be largely improved by magnetic criticality enhancement. Here, we propose and demonstrate a hybrid quantum thermometer composed of bulk diamond with ensemble  $N-V$  centers and a gadolinium magnetic flux concentrator. In addition to the magnetic criticality enhancement of gadolinium, our scheme leverages the magnetic flux concentration and ensemble  $N-V$  centers, achieving a temperature sensitivity of about  $251.5 \text{ nK}/\sqrt{\text{Hz}}$ . Near the critical point, the spin resonance to temperature ( $\partial f_{\pm}/\partial T$ ) reached  $57.3 \text{ MHz/K}$  under an external magnetic field of  $1.213 \text{ G}$ , which is about 774 times enhanced compared with that of bare  $N-V$  centers. The submicrokelvin temperature resolution of our hybrid thermometer can be used in the calibration of a reference point of temperature, integrated marine environmental surveys, laser-frequency stabilization, aerospace high-stability temperature-control systems, and many other practical applications on a macroscopic scale.

DOI: 10.1103/PhysRevApplied.21.024053

## I. INTRODUCTION

Precise temperature detection plays a crucial role in various scenarios. In addition to nanoscale temperature monitoring [1], e.g., in living cells or nanocircuits, ultra-sensitive temperature detection at the macroscopic scale is also essential, such as the calibration of a reference point of temperature [2], ultrasensitive temperature monitoring in satellites [3], laser-frequency stabilization, and integrated marine environmental surveys [4]. Macroscale thermometers with or beyond  $\mu\text{K}/\sqrt{\text{Hz}}$  sensitivity include fiber-based thermometers (fiber-loop mirror [5] and polarization-maintaining fiber [6]), resonator-based thermometers (such as whispering-gallery-mode

resonators [7–9] and Fabry-Perot resonators [10,11]), and resistance thermometers [3]. However, the fabrication of fiber-loop mirrors and Fabry-Perot resonators is complicated and expensive; the best temperature-stabilization range of a polarization-maintaining fiber is only  $10 \mu\text{K}$ ; whispering-gallery-mode resonators require precise positioning to couple the light into the resonator, limiting their applications in liquid or other complicated environments; a resistance thermometer requires complex circuits and usually suffers from electromagnetic interference [12]. Hence, a thermometer that has ultrahigh sensitivity, easy operation mode, a wide working-temperature range, and good compatibility under ambient conditions is highly desired.

Nitrogen-vacancy centers ( $N-V$  centers) [13–15] in diamond are already demonstrated to be excellent quantum sensors due to their ultralong coherence times, even under ambient conditions [16], and capability of multimodal sensing, such as magnetic fields [17–21], temperature [22–30], electric fields [31,32], and pressure [33–37].  $N-V$

\*ningwang@hust.edu.cn

†jianmingcai@hust.edu.cn

‡These authors contribute equally.

thermometry has been attractive for the past few years due to its nanoscale spatial resolution; good biocompatibility; and more importantly broad working conditions, which include a large working-temperature range from cryogenics to 1000 K [38–40], pressure range from vacuum to 140 GPa [36], and magnetic field range from zero field [41–43] to 4.2 T [44]. The N-V center in diamond is a kind of defect center, which consists of a nitrogen atom and a substitutional vacancy. The two unpaired electrons compose a spin-1 system. Due to the spin-spin interaction, there is a zero-field splitting,  $D_{GS} = 2.87$  GHz, of the ground state between  $m_s = 0$  and  $m_s = \pm 1$ , which has a temperature dependence of  $\partial D_{GS}/\partial T = -74$  kHz/K [22]. By using dedicated pulse sequences and a N-V center with a good coherence time in ultrapure diamond, the sensitivity of a single N-V center is about  $\text{mK}/\sqrt{\text{Hz}}$  [24–26]. For nanodiamonds that can work in living cells, the sensitivities are limited to about several  $\text{K}/\sqrt{\text{Hz}}$  [45–47]. All optical methods based on detection of the Debye-Waller factor of the N-V fluorescence spectrum avoid the employment of microwaves, but the sensitivities are also at the level of about  $\text{K}/\sqrt{\text{Hz}}$  [48–50].

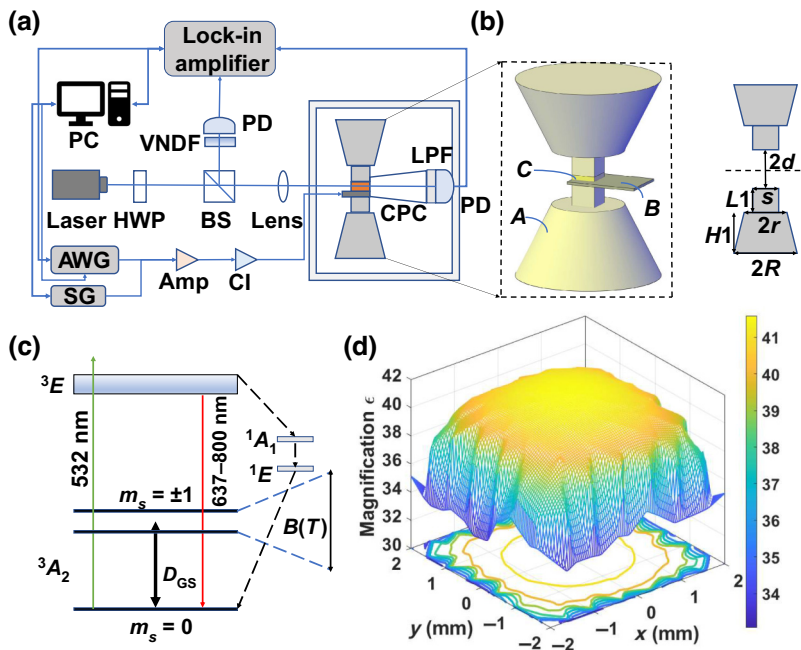
Recently, hybrid temperature-sensing schemes were proposed and demonstrated. By using the magnetic criticality of a single magnetic nanoparticle, a hybrid nanothermometer composed of a single magnetic nanoparticle and a single nanodiamond realized a sensitivity of  $11 \text{ mK}/\sqrt{\text{Hz}}$  [28]. Using a single N-V center in a diamond pillar with both bright photon counts and good coherence, the potential sensitivity of such a hybrid nanothermometer could realize about  $\mu\text{K}/\sqrt{\text{Hz}}$ . This configuration was achieved experimentally with a sensitivity of  $76 \mu\text{K}/\sqrt{\text{Hz}}$  at the nanoscale [29]. The main concept of the hybrid scheme is to transfer the temperature variation to the magnetic field to which the N-V center is most sensitive. As for N-V magnetometry, in recent work, a magnetic flux concentrator (MFC) was proposed and demonstrated to further improve the sensitivity of the magnetic field by a factor of 472 [51,52] and realized a distinguished magnetic field sensitivity of  $(195 \pm 60) \text{ fT}/\sqrt{\text{Hz}}$ .

Based on these results, we developed a hybrid sensor by combining bulk diamond containing ensemble N-V centers and a couple of magnetic concentrators made of gadolinium ( $T_C \approx 290$  K). The hybrid thermometer leverages the magnetic criticality enhancement, magnetic field concentration effect, and the large photon counts of ensemble N-V centers. Near the ferromagnetic-paramagnetic phase transition of gadolinium, the temperature sensitivity was improved by 4 orders of magnitude compared with single N-V centers in bulk diamond, resulting in a sensitivity of about  $251.5 \text{ nK}/\sqrt{\text{Hz}}$ . The MFCs amplify the magnetic flux along the N-V axis by a factor of about 14.84, achieving a dc magnetic field sensitivity of about  $31.67 \text{ pT}/\sqrt{\text{Hz}}$  as well.

## II. RESULTS

### A. Experimental setup and sensing principle

To investigate the temperature sensitivity and magnetic field sensitivity of our hybrid system, we put the whole system in a temperature chamber, as shown in Fig. 1(a). The temperature chamber was controlled by a series of thermoelectric coolers and monitored by a Pt100 temperature sensor. A Helmholtz coil was utilized to generate external magnetic fields. The configuration of the hybrid thermometer is illustrated in the inset of Fig. 1(a), which is composed of bulk diamond with ensemble N-V centers (N-V density estimated to be about 0.3 ppm, by comparing it with the photon current of a reference diamond sample with known density) and a couple of MFCs made of gadolinium (Curie temperature  $\sim 290$  K). The Curie temperature,  $T_C$ , is determined as the temperature where the magnetization susceptibility reaches its maximum value [53] (details in Sec. IV). To perform the optically detected magnetic resonance (ODMR) [13–15] measurements, we used a 532-nm green laser to excite the spin state from the side of bulk diamond and collect the photoluminescence at the other side by a photodetector (PDA100A2, Thorlabs), which is connected to a lock-in amplifier (MFLI-500 kHz, Zurich Instruments). Laser fluctuations were recorded by another photodetector with a variable neutral-density filter (VNDF) for noise cancellation. The microwaves generated by the arbitrary waveform generator (AWG5202, Tektronix) or signal generator (SSG-6000RC, Mini-Circuits) were amplified by an amplifier (ZHL-16W-43+, Mini-Circuits) and then fed into the system by a PCB board to control the spin states. The reference frequency of the lock-in amplifier (LIA) generated by AWG5202 in the experiment was set to 1 kHz in our experiments for a better signal-to-noise ratio. The geometry of the MFCs is shown in Fig. 1(b). The distance ( $2d$ ) between the two MFCs is 0.70 mm, the length ( $s$ ) of the top square cross section of the rectangular cuboid is 4 mm, and the height ( $L_1$ ) of the rectangular cuboid is 10 mm. For the conical frustum, the radius of the top ( $r$ ) and bottom ( $R$ ) and the height ( $H_1$ ) are 5, 30, and 90 mm, respectively. The MFCs concentrate the magnetic flux in a specific area. The magnification effect of MFCs depends on the shape design, the magnetic permeability of the material, and the relative position to the MFCs. For a given shape and gadolinium magnetic permeability, we could obtain the magnification factor ( $\epsilon$ ) as a function of the relative permeability, as discussed in Sec. IV. Then we used a finite-element analysis method (FEM) to simulate the magnification distribution of the transection area of the dashed line denoted in Fig. 1(b) under a relative permeability of  $\mu_r = 30$ . The simulated magnetic field distribution is uniform in a large area, as shown in Fig. 1(d). The bulk diamond ( $3 \times 3 \times 0.5 \text{ mm}^3$ ) is located in this uniform region.



Three factors contribute to the final temperature sensitivity detected by N-V centers. First, the MFCs concentrate and magnify the magnetic flux at the diamond location. Second, near the ferromagnetic-to-paramagnetic phase-transition point, the magnetic permeability of gadolinium changes significantly with temperature. Consequently, the magnification factor ( $\epsilon$ ) changes sharply with temperature, and the susceptibility  $|\partial\epsilon/\partial T|$  will reach a maximal value near the critical point. Hence, a small temperature variation can be transduced to a large magnetic field change via both MFC magnification and magnetic criticality enhancement. In addition, the sensitivity is further improved by using bulk diamond with condensed N-V centers instead of single N-V centers in bulk diamond for their brighter photon-count rates [15].

In the following, we analyze the sensitivity in detail. The ground state of the N-V center is a spin triplet with a zero-field splitting of  $D_{GS} \approx 2.87$  GHz between  $m_s = 0$  and  $m_s = \pm 1$ , even under zero field, as shown in Fig. 1(c). The spin transitions of N-V centers are shifted under magnetic fields. The simplified Hamiltonian of N-V centers can be written as

$$H = D_{GS}S_z^2 + \gamma_e \mathbf{B} \cdot \mathbf{S}, \quad (1)$$

where  $\mathbf{S} = (S_x, S_y, S_z)$  is a spin operator,  $\mathbf{B}$  is the external magnetic field amplified by MFCs, and  $\gamma_e \approx 2.803$  MHz/G is the electron gyromagnetic ratio. Note that the strain effects are ignored here as for N-V centers in bulk diamond, the strain effects are much smaller than MHz [54–56]. To measure the temperature and magnetic field simultaneously, here we use the continuous-wave (cw) method with the lock-in technique [51,52,57]. Hence, the

FIG. 1. Principle of the hybrid thermometer. (a) Illustration of the experiment device. Whole system is put into a temperature chamber controlled by thermoelectric coolers (TECs) and monitored by a Pt100 temperature sensor with proportional-integral-derivative (PID) controller with a temperature stability of  $\pm 0.05$  K. External magnetic field is controlled by a Helmholtz coils. SG (signal generator) and AWG5202 are microwave sources for measurements. PD, photodetector; HWP, half-wave plate; BS, beam-splitter; CI, coaxial isolator; LPF, low-pass filter. (b) Magnified view of the hybrid sensor. Couple of MFCs made of gadolinium, the Curie temperature of which is about 290 K. Bulk diamond with ensemble N-V center (N-V density  $\sim 0.3$  ppm) located at the center of the two MFCs, dashed gray line. (c) Energy levels of the ground states of N-V centers. (d) Simulation of the magnification distribution of the central region (transection area of the dashed gray line) under relative permeability  $\mu_r = 30$ .

sensitivity of temperature is evaluated as follows [51,52]:

$$\eta_{cw} = \delta T \sqrt{t} = \frac{\Delta L}{(d\epsilon \cos \theta / dT) B_{ext} \gamma_e L_v \sqrt{2f}}, \quad (2)$$

where  $\delta T$  is the minimum detectable temperature,  $t$  is the corresponding measurement time,  $\Delta L$  is the minimum detectable signal intensity measured under nonresonant conditions,  $\epsilon$  is the magnification factor of the MFCs,  $B_{ext}$  is the magnetic field applied by Helmholtz coils along the MFC symmetrical axis,  $\theta$  is the angle between the magnetic field and the  $z$  axis of the N-V centers,  $L_v$  is the maximum slope in the cw spectra, and  $f$  is the equivalent noise bandwidth of the system (50 Hz in our experiments).

## B. Magnification of the MFC near phase transition

First, we investigate the magnification-temperature dependence and measure the magnification at different temperatures experimentally. All the measurements are performed after the temperature inside the chamber is stable. Temperature is calibrated by the thermometer in the vicinity of the diamond. The external magnetic field generated by the Helmholtz coil current is calibrated by a flux-gate magnetometer. To obtain the magnification factor at a certain temperature, we measure the resonant frequencies,  $f_{\pm}$ , of ODMR spectra at different external magnetic fields. The resonant frequencies under an external magnetic field

are described as follows [28,58]:

$$f_{\pm} \approx D_{GS} \pm \gamma_e \epsilon B_{ext} \cos \theta \sqrt{1 + \frac{\gamma_e^2 \epsilon^2 B_{ext}^2}{4D_{GS}^2} \tan^2 \theta \sin^2 \theta} + \frac{3\gamma_e^2 \epsilon^2 B_{ext}^2}{2D_{GS}} \sin^2 \theta. \quad (3)$$

In our experiment, the external magnetic field is parallel to the [100] orientation. Hence, the angles between the  $z$  axes of all four N-V orientations and the external magnetic field are the same, namely,  $\theta \approx 54.7^\circ$ . By fitting the resonant frequencies as a function of magnetic fields with Eq. (3), we obtain the amplified axial magnetic field, which is parallel to the N-V  $z$  axis ( $B_z = \epsilon B_{ext} \cos \theta$ ). At a specific temperature, the measured axial magnetic field ( $B_z$ ) increases linearly with the increasing applied external magnetic field, as depicted in Fig. 2(a). The slope of the linear curve fitting gives the axial magnification factor ( $\epsilon_{||} = \epsilon \cos \theta$ ) of the MFC at the corresponding temperature. The measured axial magnification factors ( $\epsilon_{||}$ ) at different temperatures are summarized in Fig. 2(b). The magnification factor is associated with many parameters, such as the shape of the MFC, the relative permeability of the material, and the leakage coefficient (which is not a simple function when relative permeability is lower than 100), just to name a few. More details are shown in Sec. IV. In our case, the relative permeability changes with temperature due to demagnetization and is lower than 100, as shown in Fig. 5(d). Hence, we employ a sigmoidal function to fit the axial magnification factor as a function of temperature, as represented by the red line in Fig. 2(b).

To avoid destruction of the ODMR contrast caused by a large misaligned magnetic field [59], we carried out measurements under a small external magnetic field ( $B_{ext} = 1.213$  G). We measured the ODMR spectra at different temperatures and selected data are presented in Fig. 3(a). In Fig. 3(a), the resonant frequencies of both  $m_s = -1 \leftrightarrow m_s = 0$  (blue data and lines) and  $m_s = +1 \leftrightarrow m_s = 0$  (red data and lines) change significantly with temperature at around 290 K, indicating the significant enhancement of our hybrid scheme. The differences of the measured resonant frequencies ( $f_+ - f_-$ ) under different temperatures are plotted as black dots in Fig. 3(b). Since we have obtained the axial magnification factor as a function of the temperature in Fig. 2(b) (the sigmoidal fitting function), the difference of the resonant frequencies ( $f_+ - f_-$ ) as a function of temperature can be fitted based on Eq. (3) with the given  $\epsilon_{||}(T)$  and  $\theta$ . The fitting curve is shown as a black line in Fig. 3(b). The deviation of  $|\partial(f_+ - f_-)/\partial T|$ , obtained from the fitting curve [red line in Fig. 3(b)], reaches the maximum value at 290.2 K with a value of 114.5 MHz/K, which is about 774 times enhanced compared with that of bare N-V centers (-74 kHz/K). Note that the most sensitive temperature is 290.2 K, which is slightly different from the measured Curie temperature ( $T_C = 289.9$  K) obtained by a vibrating sample measurement (details are given in Sec. IV). We attribute such a minor difference to the fact that the magnification factor of MFCs does not change linearly with the increasing relative permeability, resulting in the temperature corresponding to the maximum susceptibility of the resonant frequencies' difference ( $f_+ - f_-$ ) being higher than the Curie temperature of Gd.

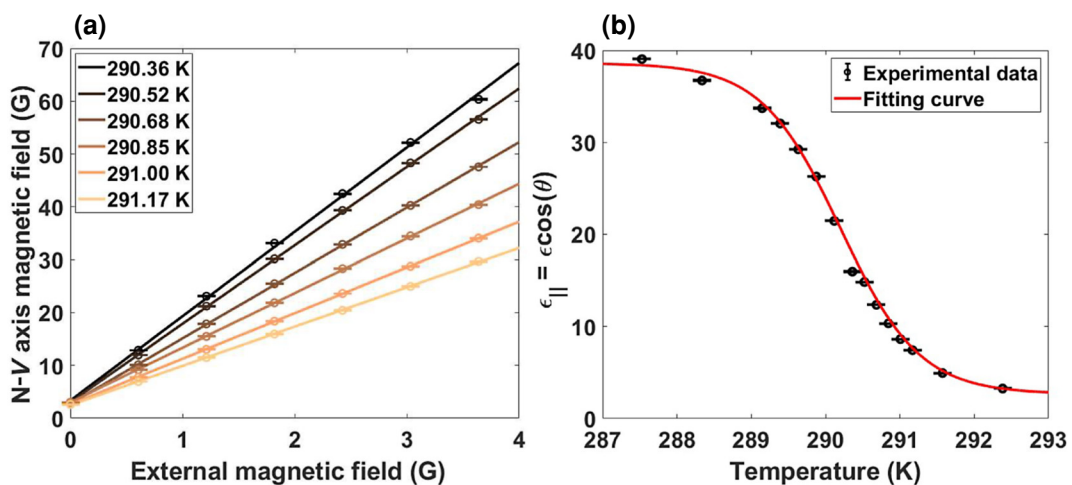


FIG. 2. Temperature dependence of magnification factors. (a) Magnification factors measured by N-V centers at specific temperatures. (b) Summary of the measured axial magnification factor as a function of temperature. Error bars indicate standard errors.

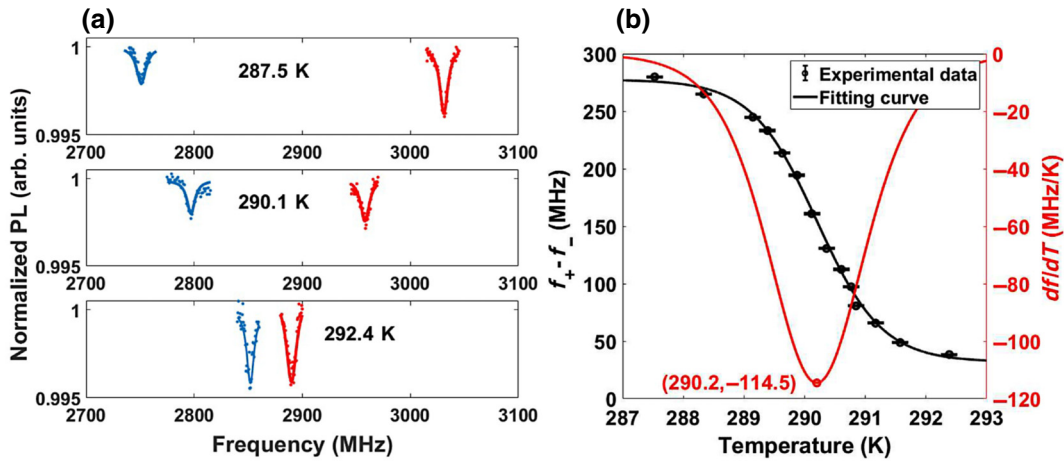


FIG. 3. ODMR measurements at different temperatures with an external magnetic field of 1.213 G. (a) ODMR spectra at different temperatures. Blue dots (line) correspond to the spin transition of  $m_s = 0 \leftrightarrow m_s = -1$  and red dots (line) correspond to the spin transition of  $m_s = 0 \leftrightarrow m_s = +1$ . (b) Energy difference (black dots and black line) between spin state  $m_s = -1$  and spin state  $m_s = +1$  as a function of temperature. Deviation of  $\partial(f_+ - f_-)/\partial T$  is illustrated as a red line. Absolute value of  $|\partial(f_+ - f_-)/\partial T|$  reaches the maximum value at 290.2 K. Error bars indicate standard errors.

### C. Magnetic field and temperature-sensitivity measurements

Then we try to experimentally demonstrate the magnetic field and temperature sensitivity of our hybrid system. We use the dual-resonance technique [52] by monitoring the spin transitions of both  $m_s = 0 \leftrightarrow m_s = -1$  and  $m_s = 0 \leftrightarrow m_s = +1$  to measure the magnetic and temperature fluctuations. The sensitivity is obtained by averaging the signal fluctuations from 10 to 50 Hz, as shown in Fig. 4(b). We experimentally measure the magnetic sensitivity at different temperatures, and then obtain the temperature sensitivity according to the susceptibility of the spin-resonance-frequency deviation to temperature,  $|\partial(f_+ - f_-)/\partial T|$ , at the corresponding temperature and

external magnetic field,  $B_{\text{ext}}$ ; see the red and black points in Fig. 4(a). The best experimental magnetic field sensitivity is 31.67 pT/ $\sqrt{\text{Hz}}$  at 290.52 K, and the best experimental temperature sensitivity is 251.5 nK/ $\sqrt{\text{Hz}}$  at 290.52 K.

### III. DISCUSSION

The sensitivity of our hybrid scheme can be further improved. First, we can use a [111]-orientated diamond sample to generate a magnetic field flux along the N-V  $z$  axis for higher ODMR contrast, even under strong magnetic fields. Second, a solid immersed lens can be fabricated at the side of diamond to further increase the

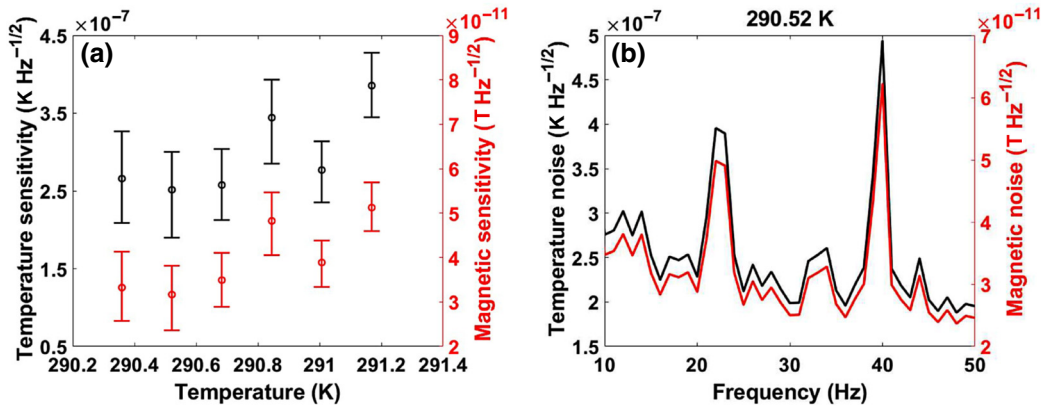


FIG. 4. Magnetic field and temperature-sensitivity measurements. (a) Measured temperature sensitivities (black dots) and magnetic field sensitivities (red dots) near the critical temperature. (b) Noise spectra from 10 to 50 Hz for the best temperature sensitivity (251.5 nK/ $\sqrt{\text{Hz}}$ , black line) and magnetic field sensitivity (31.67 pT/ $\sqrt{\text{Hz}}$ , red line) at 290.52 K in (a). Error bars indicate standard errors.

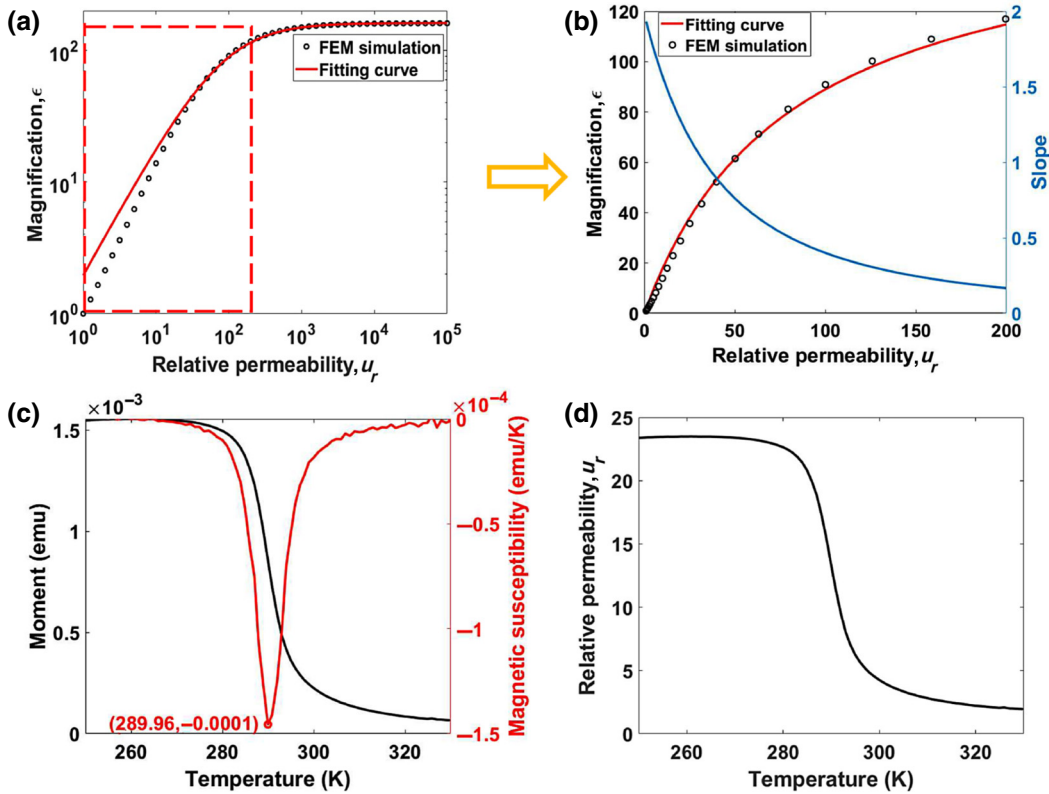


FIG. 5. Principle of MFCs. (a) Magnification of MFCs as a function of relative permeability by FEM simulation. When the relative permeability reaches 1000 or more, magnification of MFC approaches saturation. (b) Magnified data of the red dashed box in (a). Slope changes significantly when the permeability is close to 1. (c) Magnetic moment as a function of temperature under 1.3 G measured by a physical property measurement system (PPMS). Curie temperature of the gadolinium bulk is 289.96 K from the measurement. (d) Relative permeability as a function of temperature, which is derived from the curve in (c).

photon-count rate. In addition, we can use a diamond sample with higher N-V density to further improve the photon-count rate. Note that beyond a certain density, undesired interactions between different N-Vs should be considered as they could result in a rapid decay of the coherence [15]. While a recent experimental demonstration shows the feasibility to decouple these interactions with delicate design of pulse sequences [60]. In addition, further increasing the sensing volume of N-V centers through optimizing the laser excitation area and fluorescence collection volume can also improve the sensitivity for a given N-V density. Furthermore, the magnification factor can be further improved by decreasing the distance between the two MFCs with a smaller diamond sample. With these parameters optimized, the sensitivity, in principle, can be enhanced up to a level of about  $36 \text{ nK}/\sqrt{\text{Hz}}$ .

The hybrid thermometer works under ambient pressure and room temperature, so the optimized hybrid thermometer has broad applications in various fields. For example, one promising application is for temperature-reference-point calibration. It can be used to calibrate the resistance of thermistors and explore a phase-change material near room temperature. Another promising application is for

use as a prototype temperature-stabilization subsystem for a space-borne gravitational wave detector [3], laser-frequency stabilization [61], and aerospace high-stability temperature-control systems [3].

#### IV. METHODS

##### A. Setup

In our setup, the lateral face of diamond was glued onto a compound parabolic concentrator (CPC). The CPC [20,51,62] is a nonimaging optical component that can collect the photoluminescence emitted from the entire diamond sample. A lens (AC254-200-A, Thorlabs) is used to focus the 532-nm laser and the focused laser-spot radius is about  $50 \mu\text{m}$  with a depth of field of 26.5 mm longer than the side length (3 mm) of diamond. The collection volume is therefore limited by the laser-spot radius, which is estimated to be  $\pi \times 3 \times 0.05^2 \text{ mm}^3$ . The laser power used in our experiment is 50 mW (a power density of  $2 \mu\text{W}/\mu\text{m}^2$ ), which is much lower than the saturation power excitation ( $1 \text{ mW}/\mu\text{m}^2$ ) to minimize the laser heating effect. The whole setup is put into a homemade temperature chamber. A thermoelectric cooler (TEC) controlled by an AI-516

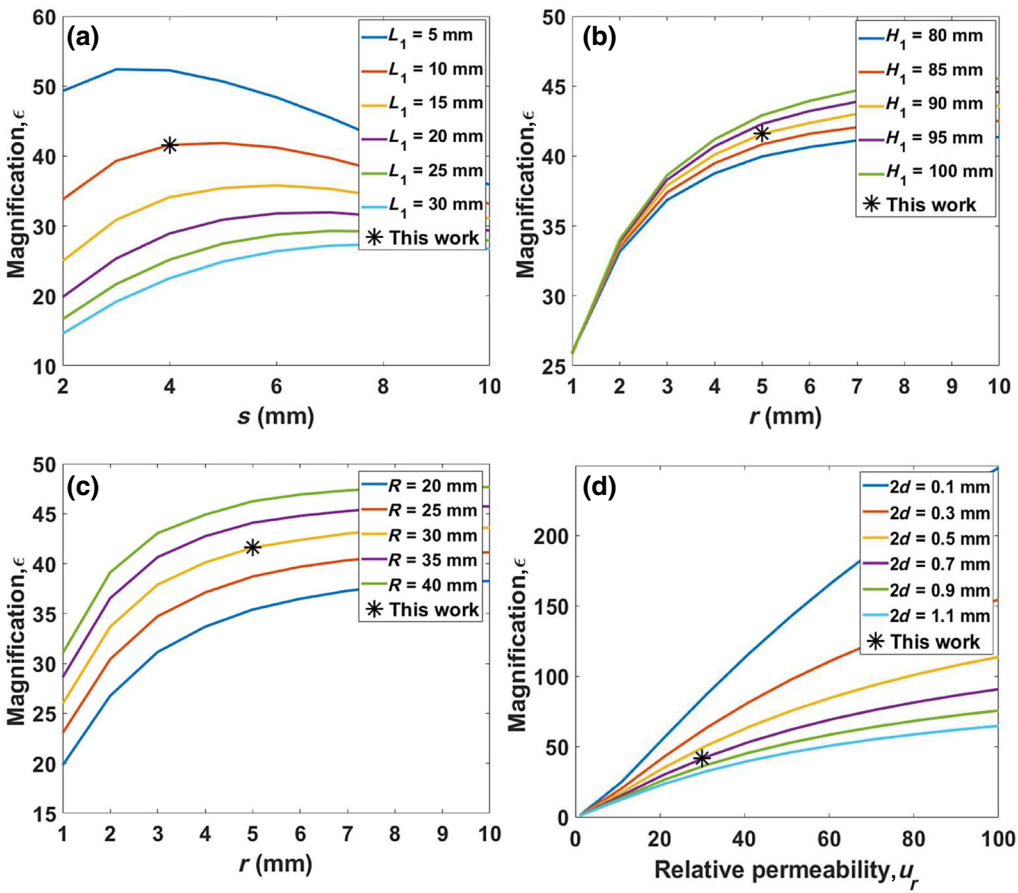


FIG. 6. Parametric FEM simulation of MFCs. (a) Magnification factor as a function of length ( $s$ ) of the square cross-section side. Different lines correspond to different values of height ( $L_1$ ) of the rectangular cuboid. (b) Magnification factor as a function of top radius ( $r$ ) of the conical frustum with different height ( $H_1$ ) of the conical frustum. (c) Magnification factor as a function of top radius ( $r$ ) of the conical frustum with different bottom radius ( $R$ ) of the conical frustum. (d) Magnification factor as a function of relative permeability with different distance ( $2d$ ) between the two MFCs. Star in each figure is the value chosen in our magnetic flux concentrator.

PID controller (Yudian Automation Technology, China) was used to control the incubator at a preset temperature; the incubator was wrapped in polyurethane foam thermal insulation panels. The heat is transferred from the TECs to a liquid cooling system. The homemade Helmholtz coil driven by the TD1605 (Suzhou TASI, China) stable current source was used to generate the magnetic field parallel to the MFC axis. The cw ODMR measurements were performed by using a signal generator. For magnetic field and temperature-sensitivity measurements, the AWG5202 was used to generate a high frequency to modulate the rf signal and reference signal for LIA at the same time. To achieve a higher sensitivity to magnetic field and temperature, different experiment settings were tested and 1-kHz modulation frequency with 1-MHz modulation depth were chosen finally.

## B. Design of MFCs

The MFCs are generally made from high relative magnetic permeability materials, such as permalloy, the

relative permeability of which is higher than tens of thousands [51]. The magnification factor,  $\epsilon$ , of MFCs of conical frustum shape can be written as [63]

$$\epsilon = \frac{B_z}{B_0} = \frac{\mu_r \beta}{(1 + N_z(\mu_r - 1))} \times \frac{\pi R^2}{s^2}, \quad (4)$$

where  $B_0$  is the external magnetic field along the  $z$  axis;  $B_z$  is the amplified magnetic field along the same direction; and  $N_z$  and  $\mu_r$  are the demagnetizing coefficient (along with the  $z$  direction) and relative permeability of the MFC, respectively.  $\beta$  is the leakage coefficient,  $s$  is the length of the square cross-section side, and  $R$  is the bottom radius of the MFC. Given the geometry of the MFC shown in Fig. 1(b), the magnification factor of the MFC depends on its relative permeability, as illustrated in Fig. 5(a). The magnification factor saturates when the relative permeability reaches 1000 or more. And it changes sharply when the relative permeability of the MFC is smaller than 100, as shown in Fig. 5(b). Here, we chose gadolinium as the MFC

material. Figure 5(c) shows the magnetic moment versus temperature [ $m(T)$ ] curve determined by vibrating sample measurements using a PPMS. The measured Curie temperature is 289.96 K. The relative permeability is related to the magnetic moment through  $\mu_r = 1 + M/H$ , where  $M$  is the volume magnetization and  $H$  is the strength of the applied magnetic field. Therefore,  $\mu_r(T)$  could be derived from  $m(T)$ , as shown in Fig. 5(d). The relative permeability of Gd in the temperature region from 250 to 330 K is lower than 100, which is in the region where the MFC changes sharply with  $\mu_r$ . Hence, the sharp magnification-factor variation, together with the sharp magnetic moment variation, contributes to the huge changes of the magnetic field at the N-V location, making gadolinium suitable for the temperature sensor in our case.

Then we consider the contribution of the demagnetization coefficient ( $N_z$ ) to the magnification factor, which is determined by the shape of the MFC. We use FEM to simulate the magnification factors with different size parameters ( $L_1, H_1, R, 2d, s, r$ ), as depicted in Fig. 6. Considering the experimental conditions, which require a uniform magnification in the diamond area and enough space for loading the CPC at the same time to achieve the highest magnification factor, the optimal parameters of our MFC are denoted as black stars in Fig. 6.

## ACKNOWLEDGMENTS

The work is supported by the National Natural Science Foundation of China (Grants No. 12161141011, No. 12304571, and No. 11874024), the National Key R&D Program of China (Grant No. 2018YFA0306600), and the Shanghai Key Laboratory of Magnetic Resonance (East China Normal University).

- [1] C. D. S. Brites, P. P. Lima, N. J. O. Silva, A. Millán, V. S. Amaral, F. Palacio, and L. D. Carlos, Thermometry at the nanoscale, *Nanoscale* **4**, 4799 (2012).
- [2] S. Rudtsch and C. von Rohden, Calibration and self-validation of thermistors for high-precision temperature measurements, *Measurement* **76**, 1 (2015).
- [3] D. Roma-Dollase, V. Gualani, M. Gohlke, K. Abich, J. Morales, A. Gonzalvez, V. Martín, J. Ramos-Castro, J. Sanjuan, and M. Nofrarias, Resistive-based micro-Kelvin temperature resolution for ultra-stable space experiments, *Sensors* **23**, 145 (2022).
- [4] Y. Zhang, D. Ye, M. Li, X. Zhang, C. Di, and C. Wang, Solid state ionics enabled ultra-sensitive detection of thermal trace with 0.001 K resolution in deep sea, *Nat. Commun.* **14**, 170 (2023).
- [5] W. Qian, C.-L. Zhao, S. He, X. Dong, S. Zhang, Z. Zhang, S. Jin, J. Guo, and H. Wei, High-sensitivity temperature sensor based on an alcohol-filled photonic crystal fiber loop mirror, *Opt. Lett.* **36**, 1548 (2011).

- [6] W. Loh, S. Yegnanarayanan, F. O'Donnell, and P. W. Juodawlkis, Ultra-narrow linewidth Brillouin laser with nanokelvin temperature self-referencing, *Optica* **6**, 152 (2019).
- [7] W. Weng, J. D. Anstie, T. M. Stace, G. Campbell, F. N. Baynes, and A. N. Luiten, Nano-Kelvin thermometry and temperature control: Beyond the thermal noise limit, *Phys. Rev. Lett.* **112**, 160801 (2014).
- [8] D. V. Strekalov, R. J. Thompson, L. M. Baumgartel, I. S. Grudinin, and N. Yu, Temperature measurement and stabilization in a birefringent whispering gallery mode resonator, *Opt. Express* **19**, 14495 (2011).
- [9] J. Lim, W. Liang, A. A. Savchenkov, A. B. Matsko, L. Maleki, and C. W. Wong, Probing 10  $\mu\text{K}$  stability and residual drifts in the cross-polarized dual-mode stabilization of single-crystal ultrahigh-Q optical resonators, *Light: Sci. Appl.* **8**, 1 (2019).
- [10] A. Reihani, E. Meyhofer, and P. Reddy, Nanokelvin-resolution thermometry with a photonic microscale sensor at room temperature, *Nat. Photonics* **16**, 422 (2022).
- [11] S. Tan, S. Wang, S. Saraf, and J. A. Lipa, Pico-Kelvin thermometry and temperature stabilization using a resonant optical cavity, *Opt. Express* **25**, 3578 (2017).
- [12] S. Dedyulin, Z. Ahmed, and G. Machin, Emerging technologies in the field of thermometry, *Meas. Sci. Technol.* **33**, 092001 (2022).
- [13] M. W. Doherty, N. B. Manson, P. Delaney, F. Jelezko, J. Wrachtrup, and L. C. L. Hollenberg, The nitrogen-vacancy colour centre in diamond, *Phys. Rep.* **528**, 1 (2013).
- [14] R. Schirhagl, K. Chang, M. Loretz, and C. L. Degen, Nitrogen-vacancy centers in diamond: Nanoscale sensors for physics and biology, *Annu. Rev. Phys. Chem.* **65**, 83 (2014).
- [15] J. F. Barry, J. M. Schloss, E. Bauch, M. J. Turner, C. A. Hart, L. M. Pham, and R. L. Walsworth, Sensitivity optimization for NV-diamond magnetometry, *Rev. Mod. Phys.* **92**, 015004 (2020).
- [16] E. D. Herbsleb, H. Kato, Y. Maruyama, T. Danjo, T. Makino, S. Yamasaki, I. Ohki, K. Hayashi, H. Morishita, M. Fujiwara, and N. Mizuochi, Ultra-long coherence times amongst room-temperature solid-state spins, *Nat. Commun.* **10**, 3766 (2019).
- [17] J. M. Taylor, P. Cappellaro, L. Childress, L. Jiang, D. Budker, P. R. Hemmer, A. Yacoby, R. Walsworth, and M. D. Lukin, High-sensitivity diamond magnetometer with nanoscale resolution, *Nat. Phys.* **4**, 810 (2008).
- [18] G. Balasubramanian, I. Y. Chan, R. Kolesov, M. Al-Hmoud, J. Tisler, C. Shin, C. Kim, A. Wojcik, P. R. Hemmer, A. Krueger, T. Hanke, A. Leitenstorfer, R. Bratschitsch, F. Jelezko, and J. Wrachtrup, Nanoscale imaging magnetometry with diamond spins under ambient conditions, *Nature* **455**, 648 (2008).
- [19] J. R. Maze, P. L. Stanwick, J. S. Hodges, S. Hong, J. M. Taylor, P. Cappellaro, L. Jiang, M. V. G. Dutt, E. Togan, A. S. Zibrov, A. Yacoby, R. L. Walsworth, and M. D. Lukin, Nanoscale magnetic sensing with an individual electronic spin in diamond, *Nature* **455**, 644 (2008).
- [20] T. Wolf, P. Neumann, K. Nakamura, H. Sumiya, T. Ohshima, J. Isoya, and J. Wrachtrup, Subpicotesla diamond magnetometry, *Phys. Rev. X* **5**, 041001 (2015).

- [21] Z. Zhao, X. Ye, S. Xu, P. Yu, Z. Yang, X. Kong, Y. Wang, T. Xie, F. Shi, and J. Du, Sub-nanotesla sensitivity at the nanoscale with a single spin, *Natl. Sci. Rev.* **10**, nwad100 (2023).
- [22] V. M. Acosta, E. Bauch, M. P. Ledbetter, A. Waxman, L.-S. Bouchard, and D. Budker, Temperature dependence of the nitrogen-vacancy magnetic resonance in diamond, *Phys. Rev. Lett.* **104**, 070801 (2010).
- [23] X.-D. Chen, C.-H. Dong, F.-W. Sun, C.-L. Zou, J.-M. Cui, Z.-F. Han, and G.-C. Guo, Temperature dependent energy level shifts of nitrogen-vacancy centers in diamond, *Appl. Phys. Lett.* **99**, 161903 (2011).
- [24] P. Neumann, I. Jakobi, F. Dolde, C. Burk, R. Reuter, G. Waldherr, J. Honert, T. Wolf, A. Brunner, J. H. Shim, D. Suter, H. Sumiya, J. Isoya, and J. Wrachtrup, High-precision nanoscale temperature sensing using single defects in diamond, *Nano Lett.* **13**, 2738 (2013).
- [25] G. Kucsko, P. C. Maurer, N. Y. Yao, M. Kubo, H. J. Noh, P. K. Lo, H. Park, and M. D. Lukin, Nanometre-scale thermometry in a living cell, *Nature* **500**, 54 (2013).
- [26] D. M. Toyli, C. F. de las Casas, D. J. Christle, V. V. Dobrovitski, and D. D. Awschalom, Fluorescence thermometry enhanced by the quantum coherence of single spins in diamond, *Proc. Natl. Acad. Sci.* **110**, 8417 (2013).
- [27] J. Wang, F. Feng, J. Zhang, J. Chen, Z. Zheng, L. Guo, W. Zhang, X. Song, G. Guo, L. Fan, C. Zou, L. Lou, W. Zhu, and G. Wang, High-sensitivity temperature sensing using an implanted single nitrogen-vacancy center array in diamond, *Phys. Rev. B* **91**, 155404 (2015).
- [28] N. Wang, G.-Q. Liu, W.-H. Leong, H. Zeng, X. Feng, S.-H. Li, F. Dolde, H. Fedder, J. Wrachtrup, X.-D. Cui, S. Yang, Q. Li, and R.-B. Liu, Magnetic criticality enhanced hybrid nanodiamond thermometer under ambient conditions, *Phys. Rev. X* **8**, 011042 (2018).
- [29] C.-F. Liu, W.-H. Leong, K. Xia, X. Feng, A. Finkler, A. Denisenko, J. Wrachtrup, Q. Li, and R.-B. Liu, Ultrasensitive hybrid diamond nanothermometer, *Natl. Sci. Rev.* **8**, nwaa194 (2021).
- [30] S.-C. Zhang, S. Li, B. Du, Y. Dong, Y. Zheng, H.-B. Lin, B.-W. Zhao, W. Zhu, G.-Z. Wang, X.-D. Chen, G.-C. Guo, and F.-W. Sun, Thermal-demagnetization-enhanced hybrid fiber-based thermometer coupled with nitrogen-vacancy centers, *Opt. Mater. Express* **9**, 4634 (2019).
- [31] F. Dolde, H. Fedder, M. W. Doherty, T. Nöbauer, F. Rempp, G. Balasubramanian, T. Wolf, F. Reinhard, L. C. L. Hollenberg, F. Jelezko, and J. Wrachtrup, Electric-field sensing using single diamond spins, *Nat. Phys.* **7**, 459 (2011).
- [32] J. Michl, J. Steiner, A. Denisenko, A. Bübau, A. Zimmermann, K. Nakamura, H. Sumiya, S. Onoda, P. Neumann, J. Isoya, and J. Wrachtrup, Robust and accurate electric field sensing with solid state spin ensembles, *Nano Lett.* **19**, 4904 (2019).
- [33] M. W. Doherty, V. V. Struzhkin, D. A. Simpson, L. P. McGuinness, Y. Meng, A. Stacey, T. J. Karle, R. J. Hemley, N. B. Manson, L. C. L. Hollenberg, and S. Prawer, Electronic properties and metrology applications of the diamond NV<sup>-</sup> center under pressure, *Phys. Rev. Lett.* **112**, 047601 (2014).
- [34] J. Cai, F. Jelezko, and M. B. Plenio, Hybrid sensors based on colour centres in diamond and piezoactive layers, *Nat. Commun.* **5**, 4065 (2014).
- [35] L. G. Steele, M. Lawson, M. Onyszczak, B. T. Bush, Z. Mei, A. P. Dioguardi, J. King, A. Parker, A. Pines, S. T. Weir, W. Evans, K. Visbeck, Y. K. Vohra, and N. J. Curro, Optically detected magnetic resonance of nitrogen vacancies in a diamond anvil cell using designer diamond anvils, *Appl. Phys. Lett.* **111**, 221903 (2017).
- [36] J.-H. Dai, Y.-X. Shang, Y.-H. Yu, Y. Xu, H. Yu, F. Hong, X.-H. Yu, X.-Y. Pan, and G.-Q. Liu, Optically detected magnetic resonance of diamond nitrogen-vacancy centers under megabar pressures, *Chin. Phys. Lett.* **39**, 117601 (2022).
- [37] R. Kitagawa, S. Nagata, K. Arai, K. Mizuno, T. Tsuji, I. Fujisaki, S. Urashita, T. Kohashi, Y. Takamura, T. Iwasaki, S. Nakagawa, and M. Hatano, Pressure sensor using a hybrid structure of a magnetostrictive layer and nitrogen-vacancy centers in diamond, *Phys. Rev. Appl.* **19**, 044089 (2023).
- [38] D. M. Toyli, D. J. Christle, A. Alkauskas, B. B. Buckley, C. G. Van de Walle, and D. D. Awschalom, Measurement and control of single nitrogen-vacancy center spins above 600 K, *Phys. Rev. X* **2**, 031001 (2012).
- [39] S. Lin, C. Weng, Y. Yang, J. Zhao, Y. Guo, J. Zhang, L. Lou, W. Zhu, and G. Wang, Temperature-dependent coherence properties of NV ensemble in diamond up to 600 K, *Phys. Rev. B* **104**, 155430 (2021).
- [40] G.-Q. Liu, X. Feng, N. Wang, Q. Li, and R.-B. Liu, Coherent quantum control of nitrogen-vacancy center spins near 1000 kelvin, *Nat. Commun.* **10**, 1344 (2019).
- [41] H. Zheng, J. Xu, G. Z. Iwata, T. Lenz, J. Michl, B. Yavkin, K. Nakamura, H. Sumiya, T. Ohshima, J. Isoya, J. Wrachtrup, A. Wickenbrock, and D. Budker, Zero-field magnetometry based on nitrogen-vacancy ensembles in diamond, *Phys. Rev. Appl.* **11**, 064068 (2019).
- [42] P. J. Vetter, A. Marshall, G. T. Genov, T. F. Weiss, N. Striegler, E. F. Großmann, S. Oviedo-Casado, J. Cerrillo, J. Prior, P. Neumann, and F. Jelezko, Zero- and low-field sensing with nitrogen-vacancy centers, *Phys. Rev. Appl.* **17**, 044028 (2022).
- [43] N. Wang, C.-F. Liu, J.-W. Fan, X. Feng, W.-H. Leong, A. Finkler, A. Denisenko, J. Wrachtrup, Q. Li, and R.-B. Liu, Zero-field magnetometry using hyperfine-biased nitrogen-vacancy centers near diamond surfaces, *Phys. Rev. Res.* **4**, 013098 (2022).
- [44] V. Stepanov, F. H. Cho, C. Abeywardana, and S. Takahashi, High-frequency and high-field optically detected magnetic resonance of nitrogen-vacancy centers in diamond, *Appl. Phys. Lett.* **106**, 063111 (2015).
- [45] D. A. Simpson, E. Morrisroe, J. M. McCoey, A. H. Lombard, D. C. Mendis, F. Treussart, L. T. Hall, S. Petrou, and L. C. L. Hollenberg, Non-neurotoxic nanodiamond probes for intraneuronal temperature mapping, *ACS Nano* **11**, 12077 (2017).
- [46] J. Choi, H. Zhou, R. Landig, H. Wu, X. Yu, S. E. Von Stetina, G. Kucsko, S. E. Mango, D. J. Needleman, A. D. T. Samuel, P. C. Maurer, H. Park, and M. D. Lukin, Probing

- and manipulating embryogenesis via nanoscale thermometry and temperature control, *Proc. Natl. Acad. Sci.* **117**, 14636 (2020).
- [47] M. Fujiwara, S. Sun, A. Dohms, Y. Nishimura, K. Suto, Y. Takezawa, K. Oshimi, L. Zhao, N. Sadzak, Y. Umemura, Y. Teki, N. Komatsu, O. Benson, Y. Shikano, and E. Kage-Nakadai, Real-time nanodiamond thermometry probing *in vivo* thermogenic responses, *Sci. Adv.* **6**, eaba9636 (2020).
- [48] T. Plakhotnik, M. W. Doherty, J. H. Cole, R. Chapman, and N. B. Manson, All-optical thermometry and thermal properties of the optically detected spin resonances of the NV<sup>-</sup> center in nanodiamond, *Nano Lett.* **14**, 4989 (2014).
- [49] T. Plakhotnik, H. Aman, and H. Chang, All-optical single-nanoparticle ratiometric thermometry with a noise floor of 0.3 K Hz<sup>-1/2</sup>, *Nanotechnology* **26**, 245501 (2015).
- [50] M. Fukami, C. G. Yale, P. Andrich, X. Liu, F. J. Hermans, P. F. Nealey, and D. D. Awschalom, All-optical cryogenic thermometry based on nitrogen-vacancy centers in nanodiamonds, *Phys. Rev. Appl.* **12**, 014042 (2019).
- [51] Y. Xie, H. Yu, Y. Zhu, X. Qin, X. Rong, C.-K. Duan, and J. Du, A hybrid magnetometer towards femtotesla sensitivity under ambient conditions, *Sci. Bull.* **66**, 127 (2021).
- [52] I. Fescenko, A. Jarmola, I. Savukov, P. Kehayias, J. Smits, J. Damron, N. Ristoff, N. Mosavian, and V. M. Acosta, Diamond magnetometer enhanced by ferrite flux concentrators, *Phys. Rev. Res.* **2**, 023394 (2020).
- [53] X. Yu, L. Wu, B. Zhang, H. Zhou, Y. Dong, X. Wu, R. Kou, P. Yang, J. Chen, C.-J. Sun, Y. Zhu, and G. M. Chow, Thickness-dependent polarization-induced intrinsic magnetoelectric effects in La<sub>0.67</sub>Sr<sub>0.33</sub>MnO<sub>3</sub>/PbZr<sub>0.52</sub>Ti<sub>0.48</sub>O<sub>3</sub> heterostructures, *Phys. Rev. B* **100**, 104405 (2019).
- [54] D. A. Broadway, B. C. Johnson, M. S. J. Barson, S. E. Lilley, N. Dontschuk, D. J. McCloskey, A. Tsai, T. Teraji, D. A. Simpson, A. Stacey, J. C. McCallum, J. E. Bradby, M. W. Doherty, L. C. L. Hollenberg, and J.-P. Tetienne, Microscopic imaging of the stress tensor in diamond using *in situ* quantum sensors, *Nano Lett.* **19**, 4543 (2019).
- [55] S. Hsieh, P. Bhattacharyya, C. Zu, T. Mittiga, T. J. Smart, F. Machado, B. Kobrin, T. O. Höhn, N. Z. Rui, M. Kamrani, S. Chatterjee, S. Choi, M. Zaletel, V. V. Struzhkin, J. E. Moore, V. I. Levitas, R. Jeanloz, and N. Y. Yao, Imaging stress and magnetism at high pressures using a nanoscale quantum sensor, *Science* **366**, 1349 (2019).
- [56] P. Kehayias, M. J. Turner, R. Trubko, J. M. Schloss, C. A. Hart, M. Wesson, D. R. Glenn, and R. L. Walsworth, Imaging crystal stress in diamond using ensembles of nitrogen-vacancy centers, *Phys. Rev. B* **100**, 174103 (2019).
- [57] A. Kuwahata, T. Kitaizumi, K. Saichi, T. Sato, R. Igarashi, T. Ohshima, Y. Masuyama, T. Iwasaki, M. Hatano, F. Jelezko, M. Kusakabe, T. Yatsui, and M. Sekino, Magnetometer with nitrogen-vacancy center in a bulk diamond for detecting magnetic nanoparticles in biomedical applications, *Sci. Rep.* **10**, 2483 (2020).
- [58] M. W. Doherty, J. Michl, F. Dolde, I. Jakobi, P. Neumann, N. B. Manson, and J. Wrachtrup, Measuring the defect structure orientation of a single NV<sup>-</sup> centre in diamond, *New J. Phys.* **16**, 063067 (2014).
- [59] J.-P. Tetienne, L. Rondin, P. Spinicelli, M. Chipaux, T. Debuisschert, J.-F. Roch, and V. Jacques, Magnetic-field-dependent photodynamics of single NV defects in diamond: an application to qualitative all-optical magnetic imaging, *New J. Phys.* **14**, 103033 (2012).
- [60] H. Zhou, J. Choi, S. Choi, R. Landig, A. M. Douglas, J. Isoya, F. Jelezko, S. Onoda, H. Sumiya, P. Cappellaro, H. S. Knowles, H. Park, and M. D. Lukin, Quantum metrology with strongly interacting spin systems, *Phys. Rev. X* **10**, 031003 (2020).
- [61] J. Lim, A. A. Savchenkov, E. Dale, W. Liang, D. Eliyahu, V. Ilchenko, A. B. Matsko, L. Maleki, and C. W. Wong, Chasing the thermodynamical noise limit in whispering-gallery-mode resonators for ultrastable laser frequency stabilization, *Nat. Commun.* **8**, 8 (2017).
- [62] H. Liang, M. Jiao, Y. Huang, P. Yu, X. Ye, Y. Wang, Y. Xie, Y.-F. Cai, X. Rong, and J. Du, New constraints on exotic spin-dependent interactions with an ensemble-NV-diamond magnetometer, *Natl. Sci. Rev.* **10**, nwac262 (2023).
- [63] P. Leroy, C. Coillot, V. Mosser, A. Roux, and G. Chanteur, An ac/dc magnetometer for space missions: Improvement of a Hall sensor by the magnetic flux concentration of the magnetic core of a searchcoil, *Sens. Actuators, A* **142**, 503 (2008).